Waveguide scattering antennas made by direct laser writing in bulk glass for spectrometry applications in the short-wave IR

M. Callejo, M. Bonduelle, A. Morand, G. Zhang, J. Lv, G. Cheng, C. D'amico, R. Stoian, G. Martin

Waveguide scattering antennas made by direct laser writing in bulk glass for spectrometry applications in the Short-Wave Infrared

M. Callejo,[1] M. Bonduelle,[2] A. Morand,[1,*] G. Zhang,[3,4] J. Lv,[3] G. Cheng,[3,4] C. d'Amico,[3] R. Stoian,[3] and G. Martin[2]

[1] Univ. Grenoble Alpes, Univ. Savoie Mont Blanc, CNRS, Grenoble INP, IMEP-LAHC, F-38000, Grenoble, France
[2] Univ. Grenoble Alpes, CNRS, IPAG, F-38400, Grenoble, France
[3] Laboratoire Hubert Curien, UMR 5516 CNRS, Université de Lyon, Université Jean Monnet, 42000 St. Etienne, France
[4] School of Artificial Intelligence, Optics and Electronics (iOPEN), Northwestern Polytechnical University, 710072 Xi'an, Shaanxi, China
[*] alain.morand@univ-grenoble-alpes.fr

Abstract: A buried straight waveguide perturbed periodically by 6 antennas composed of sub-micronic cylinder voids is entirely fabricated using ultrafast laser photoinscription. The light scattered from each antenna is oriented vertically and is detected by a Short-Wave Infrared camera bonded to the surface of the glass with no relay optics. The response of each antenna is analyzed using a wavelength tunable laser source and compared to simulated responses verifying the behaviour of the antenna. Those results show the high potential of direct laser writing technique to realize monolithic embedded detectors by combining complex optical functions within a 3D design. A wavelength meter application with a spectral resolution of 150pm is proposed to demonstrate this combination.

1. Introduction

In the recent years, it has been demonstrated that Direct Laser Writing (DLW) using ultrashort laser pulses is a powerful solution to develop integrated photonic devices [1]. DLW provides several advantages compared to the classical planar integrated optic technology. The fabrication process is first a mask-less technique avoiding the use of complex multi-step photo-lithography processes. Secondly, the focusing of an ultrashort laser pulse produces the excitation and a local change of material properties, generating an optical function based on refractive index engineering. The nonlinear absorption, limited to the focal region, gives the possibility to fabricate structures in three dimensions by repositioning the laser spot [2]. By controlling the laser pulse energy and its duration, the glass modification can be tuned from a smooth positive refractive index change (required for the waveguiding structure) to a cavitation-induced negative refractive index change creating submicronic cylinder voids [3–5]. Thus, soft excitation conditions lead to the generation of waveguiding structures until nanoscale scattering centres. This modification in the glass is also ensured by monitoring the shape of the focused light. This allows to have buried waveguides insensitive to surface evolution and to reach symmetric waveguides with a transverse Gaussian profile [6]. The refractive index contrast is rather weak (10^{-3} range), limiting the waveguide bend and the compactness of functions in the component. Nevertheless, the weak numerical aperture reduces the scattering at the output of the waveguide. With the same DLW technology and spatial beam engineering in the shape of non-diffractive Bessel beams, it is also possible to create high aspect ratio void structures with a diameter close to a few hundred nanometers [7]. These elongated void structures made in the vicinity and positioned transverse to the core waveguide can convert a small part of the light going through them into scattered light propagated in the glass wafer. Due to their high refractive index contrast ($\Delta n = n_{silica} - n_{void} = 0.45$ in fused silica), highly efficient scattering centers are made, and they are thin enough to not perturb the propagation of the light mode inside the waveguide. The use of a small cylinder void diameter is also important to ensure a correct sampling of the optical guided wave which must tend ideally to a Dirac comb function . The ability to create both 3D buried waveguides and cylindrical void based scattering centers with the same laser source is a strong advantage of the DLW technology; alternative approaches depend on complex fabrication steps that involve scanning electronic beam or focused ion beam control. Since the 2000s, the association of scattered dots set periodically along a waveguide ending with a mirror has been proposed to sample the stationary waves issued from the superposition of a forward and a backward optical waves. With a sufficient number of sampling centers (typically from one hundred to one thousand), a spectrum can be deduced after a specific Fourier transform as shown in the Stationary Wave Integrated Fourier Transform Spectrometer (SWIFTS) firstly demonstrated in a Gabor configuration [8, 9]. Additionally with a low number of sampling centers (from a dozen to twenty), a wavelength meter function can be implemented using an inverted calibration matrix [10]. In a classical approach, the structures are always made associating complex technologies: lift-off and e-beam writing to make submicron metal lines crossing silicon photonic waveguide [9] or integrated glass waveguides [11] or focused ion beam to make slot cavities in lithium-niobate waveguides [12]. In this work, the exploration of DLW is proposed as an alternative to these fabrication methods. The advantages of DLW enable time and cost efficient fabrication of robust wavelength meters. Indeed, the strengths of this technique make it especially attractive as a prototyping tool. In this work, a waveguide and several cylindrical nano-void antennas have been fabricated into a fused silica glass wafer which is then coupled to a Short-Wave Infrared (SWIR) camera to measure the intensity of the signal emitted by each antenna. The control and reproducibility of the response of each antenna measured directly on the camera is a first step before the realization of a SWIFTS by using a higher number of antennas. Despite, the low number of antennas used, another algorithm is used to reach the wavelength meter function proposed previously on niobate substrate [10]. This paper is divided in four sections. Firstly, the integrated optical device is described. Secondly, some results issued from numerical modeling are shown to preview expected results. Thirdly, optical responses obtained with a wavelength tunable laser source are shown and discussed. And finally, the calibration of this same device to work as a wavelength meter is demonstrated.

2. Device description

The device is composed of a straight waveguide finished by a metallic mirror as shown in figure 1. Light is coupled into the waveguide using the fiber set at the left side. There is a superposition of the forward wave (solid line) and the backward wave (dashed line) inducing a stationary wave inside the waveguide. As the fringe period is λ/n_g, the spatial interference pattern depends on the wavelength and the refractive index of the waveguide n_g. Periodically sampling the stationary wave can give access to the spectral information of the optical light source. Some conditions must nevertheless be respected: firstly, the sampling dot must be much smaller than the stationary wave period, linked to the minimum wavelength of the optical source. Secondly, the proportion of the extracted signal must also be weak enough to leave the stationary wave undisturbed. The efficiency of the scattering center used to convert the evanescent part of the stationary mode into radiated power depends on the refractive index change. It must be high enough to provide sufficient radiated power. Current approaches consist on nano-grooves or thin metallic stripes fabricated on the sample surface. The radiated signal is either imaged on a camera [9, 16] or the pixel array is bonded to the scattering centers to create a compact and optics-free device [11]. However, in the SWIR camera, the active area is far from the pixel physical surface (few hundred micrometers), resulting in the need for a specific design of the scattering centers to control the directivity of the radiated light in order to limit crosstalk between sampling dots [12].

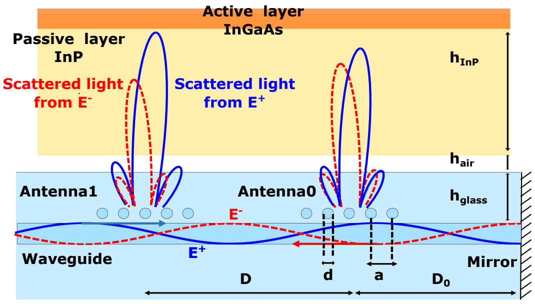

Fig. 1. Principle of the sampling centers radiating the evanescent field of the guided light toward the camera pixel without relay optic. $D = 400\mu$m is the distance between two successive antennas and $D_0 = 59\mu$m is the distance from the mirror and the first antenna depending of the manual polishing of the input facet. $a = 3\mu$m is the period of the cylinder holes in one antenna. Each one-dimensional void, transverse to the propagation axis, has a diameter $d < 200$nm. $h_{glass} \approx 50\mu$m is the reduced glass thickness between the surface and the waveguide position. $h_{InP} \approx 250\mu$m and $h_{air} = 4\mu$m. Core waveguide diameter is 50μm.

2.1. DLW features

The waveguides were fabricated in fused silica samples using an ultrafast laser photoinscription technique set in a scan configuration, with a scan of the laser spot perpendicular to the laser propagation axis. A high repetition rate (100kHz) 180fs laser radiation with an energy per pulse of 1.5μJ at 1030nm central wavelength from a Yb:KGW amplified laser system was used in a moderate focusing configuration ($NA = 0.3$). The irradiation set-up allows to simultaneously control the time and space envelope of the laser pulse by changing its spectral and spatial phase. In a fused silica wafer, where bulk refractive index is $n_g = 1.444$ at $\lambda = 1.55\mu$m, the refractive index modification obtained is in the range of $10^{-3} - 10^{-4}$. Due to the small refractive index modification, mode field diameter is large allowing to easily set a scattering center in the evanescent part without degrading the waveguide core. This technique allowing to obtain large circular cross-section waveguide photo-inscription modes is based on the method reported "beam slit-shaping" [17, 18]. In a second step, in order to generate the dielectric discontinuity useful for the scattering center, a non-diffractive irradiation procedure is used to generate a series of one-dimensional voids, transverse to the propagation axis at 3μm from the waveguide core edge, with a characteristic section below 200nm and an axial dimension above of 150μm. Diameter of 50nm has been already realized but a section of 200nm is a good compromise between reproducibility and the length part sampled . The same ultrafast Yb:KGW amplified system at a repetition rate of 100kHz, a duration of 2ps and an energy per pulse of 50μJ, is used. Instead of more common Gaussian laser beams prone to nonlinear distortion effects, picoseconds pulse Bessel beams with 10° half-cone angle (inside the material) were employed to generate enough energy concentration to trigger material cavitation. The technique allows to avoid diffraction and non linear distortions in order to create axially uniform localized uni-dimensional excitation domains inside the material. Five Bessel voids arranged at a period close to $a = 3\mu$m constitute an antenna. All these voids form a small grating to scatter light in specific directions. Ideally, the period should be $a = \lambda/n_{eff}$ to allow a scattering direction close to the vertical axis but this value is hard to obtain experimentally at the present wavelength (1.55μm) due to technical limitations. To avoid the positioning complexity when stitching the voids in a close packing, a higher order of the grating has been chosen, approximately three times higher. The consequence

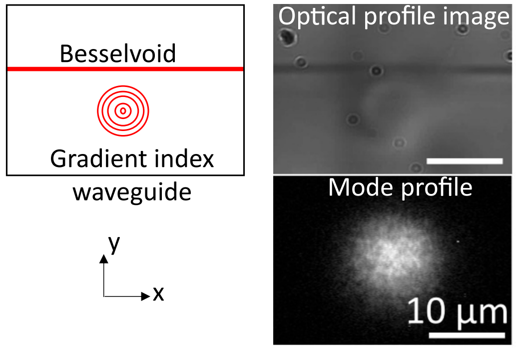

Fig. 2. Waveguide profile schematic on the surface (x, y). Optical image of the profile waveguide on the same surface with the elongated Bessel void photo-written transverse to the propagation axis (z) at 3μm from the waveguide core edge.

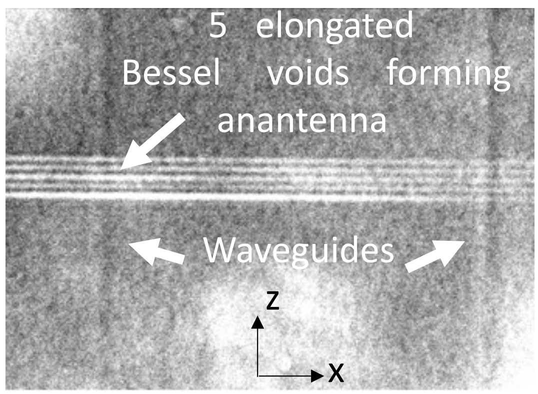

Fig. 3. Image of an antenna composed of 5 elongated Bessel voids over two photo-inscribed waveguides on the surface (xz).

is the apparition of a few Bragg orders while sampling the radiated diagram of one antenna. In figure 2, a transverse section image of the waveguide associated to elongated Bessel voids is firstly shown. With the same scale, the intensity repartition of the mode observed in the second figure is larger than the core waveguide. In figure 3, an image of one antenna realized above two waveguides is shown too. Each elongated Bessel void is made above few waveguides allowing to test different straight waveguides.

The distance $D = 400\mu$m is then set to avoid overlapping between each antenna on the detector. After the writing process, different polishing steps are done. Firstly, a polished procedure is applied at the input and output facets to access to the waveguide. Indeed, due to scattering effects perturbing the DLW process, the end and the beginning of the waveguide are made at 400μm from the initial facet. Secondly, the top surface is polished to reduce the glass thickness between the surface and the waveguide position from 400μm to approximately 50μm. It is done to avoid too much angular diffusion of the extracted beam before reaching the detector in order to reduce the crosstalk.

2.2. Set-up

The near infrared sensor used (G12242-0707W) is provided by Hamamatsu without the glass window. It is a 2D InGaAs camera with a resolution of 16384 (128×128) pixels and a pitch of

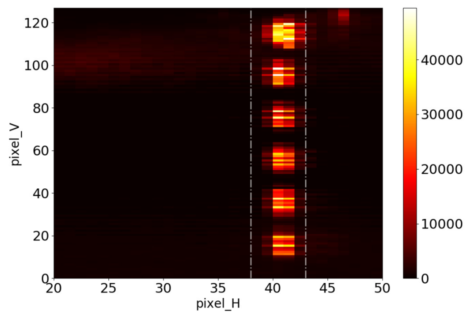

Fig. 4. Image issued from the camera at the wave number $\sigma = 6250.0\text{cm}^{-1}$ ($\lambda = 1.6\mu\text{m}$). The mirror is set at the vertical top part. The antenna 0 close to the pixel_V = 110 is the antenna set closer to the mirror. The intensity zones are associated to the scattering of each antenna. In the vertical direction, the scattering zone is enlarged due to the Bragg orders issued from the void cylinder grating. In the horizontal direction, the enlargement is smaller only associated to the waveguide mode width higher than $10\mu\text{m}$.

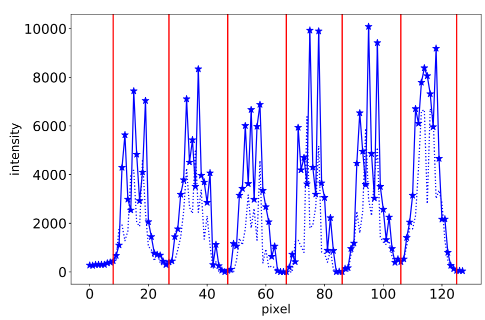

Fig. 5. Integration of the signal along the horizontal axis over few pixels. The vertical lines correspond to area boundaries of each antenna. The power of each antenna is calculated from the intensity integration over each segment. Line with marker $\star$: $\sigma = 6250.0\text{cm}^{-1}$ ($\lambda = 1.6\mu\text{m}$). Dashed line: $\sigma = 6622.5\text{cm}^{-1}$ ($\lambda = 1.51\mu\text{m}$).

20μm in a TO-8 package. An anti-reflection layer is set at the surface of the InP layer of the sensor whose thickness is approximately 250μm. All the electrical bondings and electric circuits are under the surface detector, allowing to approach the glass wafer very close to the pixels. Different micro-positioners (3D axis and rotation axis) are used to set the detector above the glass chip that is kept still by a vacuum contact. Another 3D micropositioner is used to control the fiber injection. Finally the major electric field of the polarization-maintaining fiber is oriented parallel to the void cylinders. To calibrate the device, a polarized wavelength tunable laser source is used. To scan the response of the device following the wavelength, the source's trigger output is used and connected to the trigger input of the detector. So, at each front edge of the trigger clock corresponding to a wavelength change, an image acquisition is recorded. In figure 4 and 5, an example of an image is shown. The waveguide is initially aligned to one of the sensor axis. 6 groups are clearly observed corresponding to the 6 antennas. The vertical direction is the propagation axis of the waveguide. The radiation power spreading in the transverse axis over few pixels can be observed. The 2D image is then converted in a 1D trace integrating the power detected along the transverse axis. 3 to 4 peaks are detected in each antenna group corresponding to different Bragg orders.

3. Modeling results

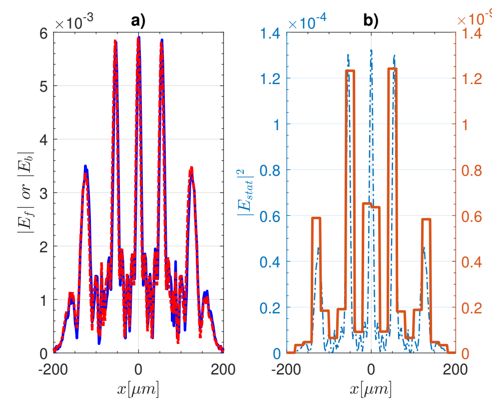

Fig. 6. a) Superposition of the forward field modulus $|E_b|$ (full line) and the backward field modulus $|E_f|$ (dashed line) of the scattering field at the detector position. b) Superposition of the stationary intensity (Dashed line) and the same intensity detected integrated on the pixels (Full line). $\lambda = 1544$nm or $\sigma = 6477$cm^{-1} with a length of 100μm between the antenna and the mirror and an hole period $a = 3.22\mu$m.

The field emitted by a single antenna is simulated with a specific home-made numerical tool. The method based on a Fourier modal decomposition is already described in [12] where it is applied to a Lithium Niobate waveguide. For the simulation, the DLW waveguide is replaced by a step-index waveguide: a core waveguide with a thickness of 2μm and a refractive index of 1.446 surrounded by a refractive index of 1.444. The glass thickness between the glass wafer surface and the core waveguide is 50μm. Since the image sensor is not in direct contact with the glass surface, a 4μm air gap is included between the glass and the InP layer. The thickness of the passive InP layer before the camera active layer is equal to 250μm. The shape of the holes is approximated by a square (100nm × 100nm) filled with air. Due to the size of the multilayer, 801 harmonics are chosen in the fully vectorial tool used in the first step to ensure the convergence. A length of 100μm is set between the mirror and the antenna center. This distance has been chosen in order to be able to properly sample the stationary wave intensity in a wavelength range

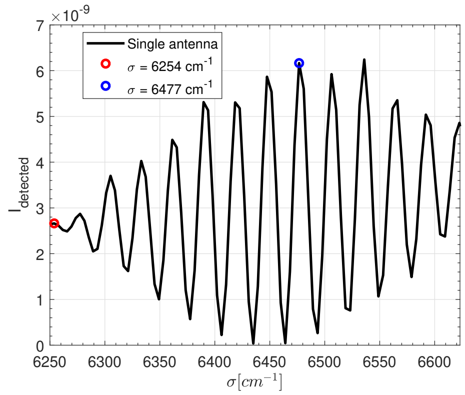

Fig. 7. Evolution of the intensity of one antenna as a function of σ with a length of 100μm between the antenna and the mirror and an hole period $a = 3.22\mu$m. Optimal case with one fringe packet or one lobe of the envelope.

from 1510nm to 1600nm or a wave number from 6250cm^{-1} to 6623cm^{-1}. Finally, the mirror is considered perfect with an amplitude reflection $r = -1$. The modelization of the far radiated field in the active zone of the detector is made in two steps. First of all, the radiation pattern in the first micrometers of the InP layer is numerically modeled with a 2D Aperiodic Fourier Modal Method (AFMM) in guided configuration [13]. The electromagnetic (EM) fields were calculated along a line parallel to the waveguide propagation axis in the InP layer 0.5μm above the interface InP layer. Secondly, the radiation pattern of the light diffracted in each antenna was extrapolated into the far field with the Helmholtz - Kirchhoff diffraction theory [14, 15] in which the Green function is approximated by an exponential one instead of Hankel functions . An antenna of 5 voids with a period of $3\lambda/n_g = 3.22\mu$m is firstly simulated corresponding to the ideal case (hole period exactly matching a multiple of λ/n_g). In figure 6, different scattered field moduli are shown in the detector area. In this optimized case, the forward and backward field modulus (on the left figure) are well superposed ensuring a high contrast of the stationary wave intensity (on the right figure). In this last figure, the intensity evolution detected by each pixel (full line) is also shown. The scattered light is composed of 5 Bragg orders. The width of each Bragg peak is proportional to the number of voxels in a single antenna and its shape can be approximated by a sinus cardinal function, whereas the envelope evolution is linked to the average shape of the voxel chosen. The positions of the peaks are dependent on the wavelength. If the wave number is decreased, the forward scattered field is not symmetric any more, reducing its overlapping with the backward scattered field. The contrast issued from the intensity calculation in this case decreases as shown in figure 7. A worse case can be reached when the wave number is close to $\sigma = 6250$cm^{-1} where a zero of the forward scattered field is superposed to a maximum of the backward scattered field. For smaller wave number, a new fringe packet can appear but with a smaller envelope contrast. Indeed, this effect can be observed when voxel period a is reduced: the results for $a = 3\mu$m are shown in figure 8 and figure 9. The Bragg order maxima are clearly separated. Nevertheless, an overlapping is always possible but the forward and backward field amplitudes are highly different. The principal sinus cardinal lobe of the forward field is located on the secondary lobe of the backward field with a smaller amplitude. Each previous peak of the intensity evolution are separated in two peaks (one from the forward wave and the other from the backward wave). A fringe packet can be observed but the contrast maximum calculated at 90% in the optimized case falls at 20% in this case. As the period achieved with the DLW method is closer to $a = 3\mu$m rather than $a = 3.22\mu$m, all the contrast results shown in the next part are affected by the non-optimized hole period.

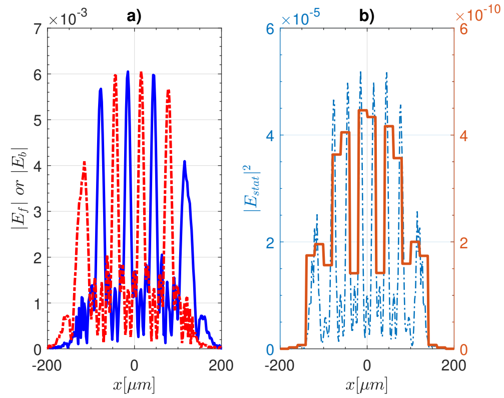

Fig. 8. a) Superposition of the forward field modulus $|E_b|$ (full line) and the backward field modulus $|E_f|$ (dashed line) of the scattering field at the detector position. b) Superposition of the stationary intensity (Dashed line) and the same intensity detected integrated on the pixels (Full line). $\lambda = 1579$nm or $\sigma = 6333\text{cm}^{-1}$ with a length of 100μm between the antenna and the mirror and an hole period $a = 3\mu$m.

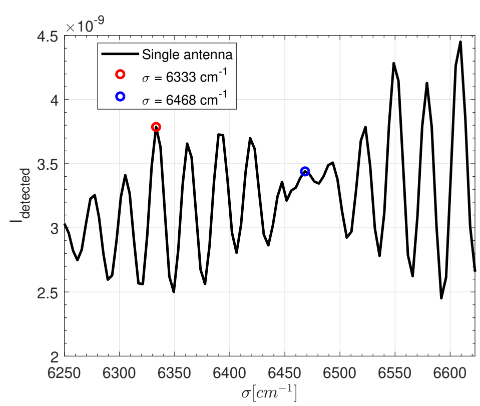

Fig. 9. Evolution of the intensity of one antenna as a function of σ with a length of 100μm between the antenna and the mirror and a hole period $a = 3\mu$m. Sub optimal case with two fringe packet or a zero between the lobes of the envelope.

4. Antenna response measure versus wave number

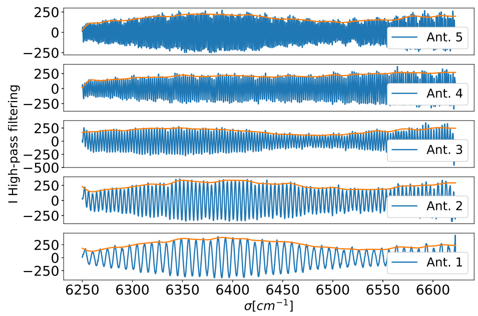

Fig. 10. Intensity response of each antenna after pixel integration as a function of the wave number (except the antenna 0 which is disturbed by the mirror reflection). The modulated evolution has been previoulsy filtered by a Butterworth band-pass filter, and the envelope signal is issued from the Hilbert transform followed once again by a Butterworth low-pass filter.

To obtain the power emitted by each antenna, the profile shown in figure 5 must be split in 6 segments of width $D = 400\mu m$ defined by the successive vertical lines. The power in each zone is then integrated to define the radiated power $P_i(\sigma)$ emitted by the antenna i. Using a tunable source, the wavelength is swept from 1510nm to 1600nm with a step of 10pm. The evolution of the $P_i(\sigma)$ signal is a combination of a periodical oscillation (the interference signal) with an amplitude envelope and a wavelength dependent offset (mean value of the oscillation). The analysis of this signal can be used to obtain useful insight into the properties of the scattering centers fabricated using the DLW technique. The first step for the analysis of the signal is to separate the mean value from the interference signal. This is achieved by means of a Butterworth band-pass filter applied twice (equivalent to a filter of order 8 and zero delay) to avoid ripples in the bandwidth zone. This treatment is coded in Python using the function butter issued from the library scipy.signal. With a wavelength step of $\Delta lambda$ = 20pm (or $\Delta sigma$ = 0.083cm^{-1}), the low and high cut-off frequencies used as inputs are respectively $0.05/f_{max}$ and $2/f_{max}$ with $f_{max} = 1/(2\Delta sigma)$. The result of the filtering is shown in figure 10. The oscillation period of each antenna is directly related to the distance between the antenna and the mirror: the period decreases as the distance to the mirror increases. The envelope can be extracted by means of a Hilbert transform followed by a low-pass filter to remove ripples from the result. The envelope of the oscillation is shown in figure 11.

The envelope evolution shape depends on the number of void cylinders used in a single antenna. As the hole period is close to $a = 3\mu$m, the overlapping between the forward and backward scattered fields before the intensity conversion is not optimized, reducing the contrast of the fringe packet observed as shown in the modelization section in figure 9. The optimized fringe packet is expected to be centered at the wave number 6925cm^{-1}, outside of the wave number range observed. In theory, a zero contrast is expected between two successive fringe packets. This zero appears if all voids are identical (same shape and same size). If they are not, the scattering of one Bragg order is modified and the narrow peak evolution is not a sinus cardinal function anymore. This result can induce an overlapping change between the forward and backward fields. Having different hole sizes in a single antenna can be seen as an apodization of the fringe packet, leading to the removal of the zero contrast. A simulation has been made choosing 5 holes with the following arbitrary widths of 100, 140, 120, 200 and 180nm instead of the single width of 100nm used in the modelization part. The intensity evolution of an antenna following the wave

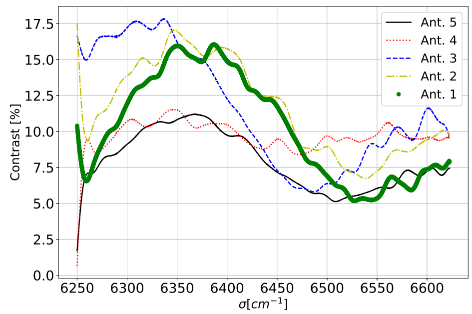

Fig. 11. Evolution of the contrast issued from the previous envelopes as a function of the wave number. The number in the legend is associated to the antenna i studied.

number is given in figure 12 for a period $a = 3\mu$m. The contrast evolution calculated becomes smoother than the single hole width case and always remains far from 0. It is clearly a hole width dispersion which can explain the contrast evolution measured.

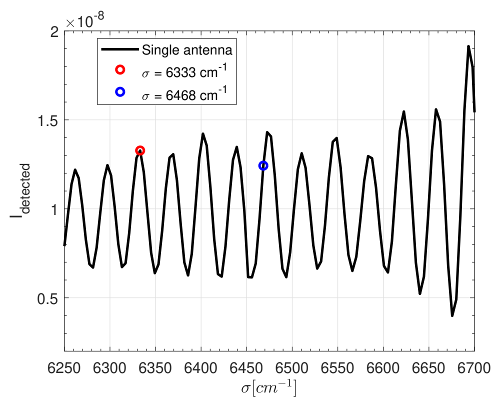

Fig. 12. Intensity evolution as a function of σ simulated for one antenna with a length of 100μm between the antenna and the mirror, and an hole period $a = 3\mu$m. Effect of manufacturing non uniform holes: 5 holes with the following widths 100, 140, 120, 200 and 180nm instead of having uniform holes with a width of 100nm. The envelope amplitude no longer goes to zero between two successive fringe packets or lobes.

A maximum contrast of 17.5% is obtained from the measurement of the device. This contrast is slightly smaller than the predicted value of 19% for the case of identical holes of width 100nm. This maximum contrast changes from one antenna to another. It depends on the fabrication accuracy but also on the differential loss between both the forward and backward waves. Indeed, the interference is maximized when the two waves have the same amplitude. However, due to the different path followed and the signal extracted by the neighboring antennas, this configuration changes from one antenna to another.

Nevertheless, the minimum contrast position should be the same for each antenna if dispersive effects in the waveguide are neglected. As shown in figure 9 and figure 7, this position depends on the voxel period of the antenna and can be used to analyze the reproducibility of the void cylinder period in each antenna. A wave number shift can be observed, which is analysed in figure 13. The diamond corresponds to simulated minimum position using the previously mentioned numerical

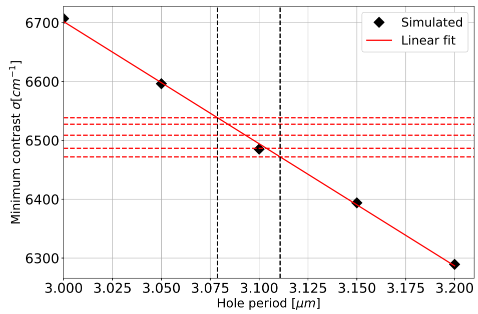

Fig. 13. Evolution of the simulated minimum contrast position as a function of the period of the cylinder holes. The horizontal lines correspond to the measured values issued from the 5 previous antennas characterized. The vertical lines are respectively an estimation of the minimum period and of the maximum period of the antennas realized.

tool [12]. The horizontal lines added on the figure are the minimum contrast wave number issued from the previous measurements of the 5 characterized antennas. The period a of the void cylinder is estimated between 3.078μm and 3.111μm. The accuracy of this period is ±35nm. This evolution can also appear in a single antenna.

5. Fast Fourier transform of the previous signals

From the intensity evolution as a function of the wave number, the position of each antenna can be obtained using a Fast Fourier transform. A Welch [19] method has been chosen in association with a Bartlett-Hann window and a padding method (4 more sampling elements). The Welch's method computes an estimate of the power spectral density by dividing the data into overlapping segments, computing a modified periodogram for each segment and averaging the periodograms. And to limit the ripples in the frequency domain after a Fourier transform due to a rectangular window, a triangular window is used for tapering the signal. The noise is reduced at the expense of the resolution. The spectrum for each antenna is normalized by its maximum value and shown in figure 14. Each graph on the figure is the superposition of each single antenna's spectrum. The peak position gives the spatial position of the antenna. Crosstalk appears if the signal of one antenna shows at the position of another antenna. Spectra of the 5 antennas for different laser polarizations are shown. The separation D between each antenna associated to the single antenna scattering allows to obtain a low crosstalk between each antenna in the TE polarization case. Changing the polarization state, the crosstalk increases with the apparition of peaks with non-negligible amplitudes at wrong positions. This is due to the radiated diagram of the TM case cancelling the vertical propagation direction. The highest crosstalk is observed on the last two antennas. However this effect remains reasonable in our case. It is worth noting that the separation between the antennas is enough to record a major part of the TM radiated diagram. For smaller separation, the device will be more sensitive to the polarization. Each peak is then close to a Gaussian shape which can be used to fit each of them. In this way, the antenna position can be determined with an accuracy close to a few micrometers as shown in Table 1. From a linear fit of the antenna position versus the antenna number, it is notably interesting to determine the distance D_0 between the first antenna and the mirror as well as the spatial separation D between two successive antennas. Indeed, the value of D_0 is difficult to determine precisely after the polishing steps. The respective values calculated from the fitting are $D = 402 \pm 1\mu$m and $D_0 = 59 \pm 2\mu$m.

6. Wavelength meter

Spectral information can be extracted from our system with a reduced number of antennas. Therefore, all the pixels analysed along a propagation axis line are used to define a calibration matrix with a first wavelength scan from 1510nm to 1600nm and a step of 40pm. This calibration gives a matrix with a shape $N_{Pixel} \times N_\lambda$ with $N_{Pixel} = 128$ the pixel number along a line and $N_\lambda = 1751$ the number of scanned wavelengths. The intensity pixel vector I_p measured can then be linked to the wavelength vector to find λ as $I_p = M\lambda$. Two methods are then proposed. The first one is a least mean square solution to minimize the norm $|I_p - M\lambda|^2$. The second solution consists in directly calculating $M_f^{-1} I_p$ and select the maximum value. M_f is not the inverted matrix of M but the pseudo inverse matrix where all values smaller than $r_{cond}.\max(SVD)$ are forced to zero with $1 \geq r_{cond} \geq 0$ and SVD a vector containing the singular values of M. The value of the cutoff has been manually chosen to be $r_{cond} = 0.4$.

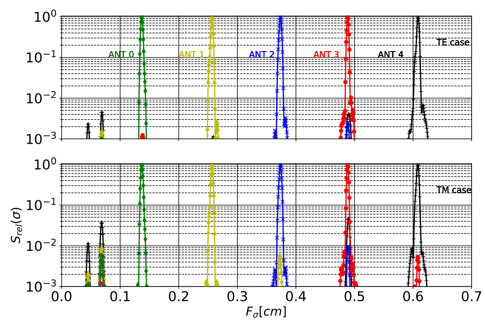

Fig. 14. Spectrum of the intensity evolution for different polarization states. $S_{rel}(x) = \sum S_{rel,i}(x)$ and $S_{rel,i}(x)$ is the power issued from the antenna i and normalized as $S_{rel,i}(x) = P_{Ant,i}(x)/max(P_{Ant,i}(x))$. From the up, the first and the second graphs are respectively for the TE polarization (0°) and TM polarization (90°) cases. Each peak is associated to the response of a single antenna studied.

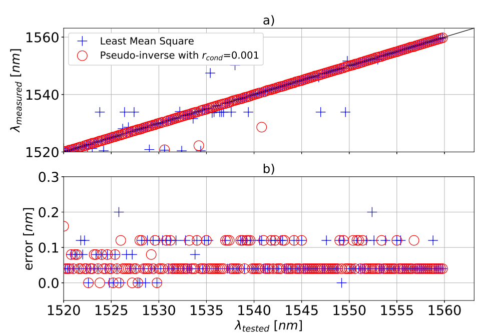

Fig. 15. a) Comparison of the two methods used to analyse the wavelength meter efficiency (Least mean square method and Pseudo inverse matrix method with $r_{cond} = 0.001$. b) Evolution of the error between the reference and the wavelength tested.

The effectiveness of these methods has been tested by using another wavelength sweep measurement, performed under the same conditions but with a different wavelength step of 200pm, from 1520nm to 1560nm. The results of both methods are shown in figure 15. Some cases are not well restored by both methods, and in particular for the least squares approach (+ markers). There are more + markers than ∘ markers. But the pseudo inverse method seems to be more efficient notably for wavelengths higher than 1540nm. It is noteworthy that the error is under 0.15nm in the wavelength range observed despite the limited number of antennas. To improve this method with the same antenna number, it would be more interesting to use antennas with different period, size ... This is a first step to analyse and confirm the response of this radiated power extraction solution to sample the stationary wave of an integrated waveguide.

n	1	2	3	4	5	Error
$f/2n_g$ $[\mu m]$	467	872	1277	1686	2091	±10

Table 1. Evolution of the spatial peak position issued from the intensity evolution spectrum.

Conclusion

A novel approach to signal sampling using DLW voxels and waveguides has been proposed. It is demonstrated that each scattering center, made by a group of parallel and periodic elongated Bessel nano-voids (an antenna), is able to transversally scatter a signal which is proportional to the integrated optic stationary wave inside the waveguide at a given discrete position from the end mirror. The measured spectral response is close to the expected response. The wavelength scan can be used to give information about the morphology of the Bessel nano-voids. The reproducibility of the DLW technology is from our point of view sufficient to test it along a longer waveguide with a higher number of antennas in order to implement a SWIFTS. However, in order to increase the contrast and have a more compact device, the period of the nano-voids forming an antenna must be chosen closer to $p\lambda/n_{eff}$ with p an integer. In this paper, the achieved period is close to $a = 3.1\mu$m nm rather than $a = 3.22\mu$m, thus inducing a change of Bragg orders and limiting the contrast to 17.5% instead of an expected value close to 90% in the optimized case. For future improvements the challenge will be the reduction of this period to $p = 1$, In this case, only one Bragg order will be excited by an antenna ensuring high contrast, large wavelength bandwidth to analyse and reduced cross-talk.

Funding. The authors acknowledge funding from ASHRA (Action Specifique Haute Resolution Angulaire) from INSU-CNRS, LabEx FOCUS ANR-11-LABX-0013 and LabEx Manutech-SISE ANR-10-LABX-0075. G. Zhang acknowledges China Scholarship Council fellowship.

Disclosures. The authors declare no conflicts of interest.

References

1. K. M. Davis, K. Miura, N. Sugimoto and K. Hirao "Writing waveguides in glass with a femtosecond laser," Opt. Lett. **21**, 1729–1731 (1996).
2. A. Rodenas, G. Martin, B. Arezki, N. Psaila, G. Jose, A. Jha, L. Labadie, P. Kern, A. Ajoy and R. Thomson "Microstructuring of Nd: YAG crystals by proton-beam writing," Opt. Lett. **37** 392–394 (2012).
3. M. K. Bhuyan, F. Courvoisier, P. Ã. Lacourt, M. Jacquot, R. Salut, L. Furfaro and J. M. Dudley "High aspect ratio nanochannel machining using single shot femtosecond Bessel beams," Appl. Phys. Lett. **97** 081102 (2010).
4. M. Bhuyan, P. K. Velpula, J. P. Colombier, T. Olivier, N. Faure and R. Stoian "Single-shot high aspect ratio bulk nanostructuring of fused silica using chirp-controlled ultrafast laser Bessel beams," Appl. Phys. Lett. **104** 021107 (2014).
5. R. Stoian, M. Bhuyan, G. Cheng, G. Zhang, R. Meyer, and F. Courvoisier "Ultrafast Bessel beams: advanced tools for laser materials processing," Adv. Opt. Technol. **7** 165–174 (2018).
6. C. D'Amico, G. Cheng, C. Mauclair, J. Troles, L. Calvez, V. Nazabal, C. Caillaud, G. Martin, B. Arezki, E. LeCoarer, P. Kern and R. Stoian "Large-mode-area infrared guiding in ultrafast laser written waveguides in Sulfur-based chalcogenide glasses," Opt. Express **22** 13091–13101 (2014).

7. Zhang Z., Cheng G., Bhuyan M., D'Amico C. and Stoian R. "Efficient point-by-point Bragg gratings fabricated in embedded laser-written silica waveguides using ultrafast Bessel beams," Opt. Lett. **43** 2161–2164 (2018).
8. Thomas F., Heidmann S., De Mengin M., Courjal N., Ulliac G., Morand A., Benech P., Le Coarer E. Martin G. "First results in near and mid IR lithium niobate-based integrated optics interferometer based on SWIFTS-Lippmann concept," J. Light. Technol., **32** 3736–3742 (2014).
9. Le Coarer E., Blaize S., Benech P., Stefanon I., Morand A., Lerondel G., Leblond G., Kern P., Fedeli J-M and Royer P. "Wavelength-scale stationary-wave integrated Fourier-transform spectrometry," Nat. Photonics **1** 473–478 (2004).
10. Bonduelle M., Heras I., Morand A., Ulliac G., Salut R., Courjal N. and Martin G. "Near IR stationary wave Fourier transform lambda meter in lithium niobate: multiplexing and improving optical sampling using spatially shifted nanogroove antenna," Appl. Opt. **19** D83–92 (2021).
11. Bonneville C., Thomas F., De Mengin Poirier M., Le Coarer E., Benech P., Gonthiez T., Morand A., Coutant O., Morino E., Puget R. and Martin B. "SWIFTS: a groundbreaking integrated technology for high-performance spectroscopy and optical sensors," Proceeding SPIE MOEMS Miniaturized Syst. XII **86160M** (2013).
12. Morand A., Heras I., Ulliac G., Le Coarer E., Benech P., Courjal N and Martin G. "Improving the vertical radiation pattern issued from multiple nano-groove scattering centers acting as an antenna for future integrated optics Fourier transform spectrometers in the near IR," Opt. Lett. **44** 542–545 (2019).
13. Bucci D., Martin B. and Morand A. "Application of the three-dimensional aperiodic Fourier modal method using arc elements in curvilinear coordinates," J. Opt. Soc. Am. A **29** 367–373 (2012).
14. Marcuse D. "Light Transmission Optics," (Van Nostrand Rinhold Company) (1972).
15. Martin B., Morand A., Benech P., Leblond G., Blaize S., Lerondel G., Royer P., Kern P. and Le Coarer E. "Design of a new compact Static Fourier Transform Spectrometer in integrated optics based on a leaky loop structure," Opt. Lett. **34** 184–186 (2009).
16. Pohl D., Escalé M. R., Madi M., Kaufmann F., Brotzer P., Sergeyev A., Guldimann B., Giaccari P., Alberti E., Meier U. and Grange R. "An integrated broadband spectrometer on thin-film lithium niobate," Nat. Photonics **14** 24–29 (2020).
17. Cheng Y., Sugioka K., Midorikawa K., Masuda M., Toyoda K., Kawachi M., Shihoyama K. "Control of the cross-sectional shape of a hollow microchannel embedded in photostructurable glass by use of a femtosecond laser," Opt. Lett. **28** 55-–57 (2003).
18. Osellame R., Taccheo S., Marangoni M., Ramponi R., Laporta P., Polli D., De Silvestri S., Cerullo G. "Femtosecond writing of active optical waveguides with astigmatically shaped beams," J. Opt. Soc. Am. B **20** 1559-–1567 (2003).
19. Welch P. "The use of fast Fourier transform for the estimation of power spectra: a method based on time averaging over short, modified periodograms," IEEE Transactions on audio electroacoustics **15** 70–73 (1967).